Short-term cathodic tuning atomic-level S-S interaction of CuS for heavy metal ultrafast detoxication

Liming Yang [a], Guangzhen Liu [a,b], Zhenglin Chen [a], Zhiyan Guo [c,d], Tian Liu [c,d,*], Hui Shi [a], Penghui Shao [a], Xianchuan Xie [b], Wenwei Li [c,d], Xubiao Luo [a,e,**]

[a] National-Local Joint Engineering Research Center of Heavy Metals Pollutants Control and Resource Utilization, Nanchang Hangkong University, Nanchang, Jiangxi 330063, PR China
[b] School of Resources and Environment, Nanchang University, Nanchang, Jiangxi 330031, PR China
[c] University of Science and Technology of China, Hefei 230026, PR China
[d] Suzhou Institute for Advanced Research, University of Science and Technology of China, Suzhou 215123, PR China
[e] School of Life Science, Jinggangshan University, Ji`an 343009, PR China

ABSTRACT

Transition metal sulfides have demonstrated excellent heavy metal detoxification in previous studies. However, the activity of their S-functional sites is usually not maximized because they are not precisely regulated. Herein, we report a new short-term cathodic tuned CuS crystals (C-tuned CuS) distortion strategy, ultrafast detoxicating over 95% Cr(VI) in 1 min , its detoxification rate was elevated by five orders of magnitude times compared to the untuned one. The high Cr(VI) detoxification performance is mainly attributed to the layered sulfur atoms tuning within series of cathodic potential shown by In-situ Raman. Besides, the four-tuning stages of C-tuned CuS lattice distortion based on the variation of Raman peak height and redshift changes was investigated by density functional theory (DFT) calculations, showing that the S-S bonds was stretched under cathodic tuning, extending from 2.106 to 2.345 Å. The stretched S-S bonds with enhanced polarity and electron activity prevailed the formation of transient Cr-S bonds with Cr(VI), favoring the direct electron transfer without O mediation, thus reducing the Cr(VI) reduction energy barrier. Cathodic tuning CuS crystal distortion, a "Plug and Play" strategy, show a new electron-level microscopic insights into wastewater reduction techniques development.

1. Introduction

Metal-sulfate nano particle has been wildly reported in the heavy metal reduction detoxication. [1–3] Compared with the traditional zero-valent metal like Fe(0), sulfate layer may tune the surface electron flow and accumulation, forming an 'electron donor-surface mediation' micro-electron transfer system. [4,5] Besides the sulfate layer can further enhance the particle surface area and prevent the nano-particles aggregation. Although the metal-sulfate shows a considerable prospect in the future environmental protection, the sulfate mediation layer cut down the direct electron transfer connection between the heavy metal ion and zero-valent metal, inhibiting the reduction overpotential and activity in theory. [6,7] As a result, developing surface structure tuning strategy may further max the metal-sulfate reduction performance.

Several reports show that the sulfate atom and around atomic interactions including S-S and M-S bond seriously influence the surface kinetics. [8–10] For example, Xu et al. [11] constructed a 1 T′ $Re_{1-x}Mo_xS_2$ catalyst for rapid hydrogen precipitation, which induced the formation of a unique electron-deficient channel-sulfur site by weakening the Re-Re bond strength through the introduction of Mo, resulting in thermally neutral S-H bonding and achieving excellent interfacial H_2 generation performance. Thus, the accurate sulfate tuning strategies shows a great significance in enhancing the metal-sulfate reduction activity. [12] Current sulfate site tuning mainly concentrate on phase changing, constructing sulfate detection and doping. [13–16] However, these strategies can hardly tune the atomic interactions around sulfate in a high accuracy. Besides, these strategies usually use toxic agent like hydrazine hydrate or high temperature and pressure,

[17,18] showing secondary pollution and high carbon emission. Thus, new sulfate accurate and green tuning strategy is urgent needed for further enhancing the surface sulfate reduction performance.

Considering that in-built electric field is the main appearance result of atomic structure tuning. In theory, one promising strategy is using additional electric field to tune the M-S or S-S bond. [18,19] Ideally, the atoms and electron distribution will reach a new equilibrium under a considerable additional electric field. Specially, metal sulfate like CuS, ZnS may have a well atom micro-structure tuning performance under the electric field due to the easily distortion of crystal lattice. [20–24] Besides the layered structure with "soft" S-S bond with different obits for accommodating electrons makes it easily to be regrouped (Fig. S1). Till now few works reported adding electric field tuning the atomic structure of metal sulfate for enhancing the chemical reduction activity.

Herein, we firstly reported a cathodic atomic sulfate tuning strategy of CuS, achieving over 95% Cr detoxication in 1 min without any inducing energy and additional agent during the treatment. The high performance of Cr detoxication is attributed to a simple and environment friendly method, 3-min short term cathodic tuning, driving layered S atom distortion in CuS, seriously reducing the reduction energy barrier. The in-situ Raman assisted with density functional theory (DFT) calculation was employed for clearly showing the 4 stages of CuS distortion within cathodic potential. Atomic scale accuracy and environmental friendly of cathodic tuning method shows it a "Plag and Play" strategy, offering a new insight into the wastewater reducing treatment technology development.

2. Methods

2.1. Reagents and materials

All reagents were used as received from the manufacturer, blue copperas ($CuSO_4 \cdot 5 H_2O$, ≥99%), acetone (CH_3COCH_3, 99.5%), sulphuric acid (H_2SO_4, 95–98%), sodium hydrate (NaOH, ≥96%), sodium sulfate (Na_2SO_4, ≥99%), nitric acid (HNO_3, 36–38%), potassium dichromate ($K_2Cr_2O_7$, ≥98%) were purchased from Aladdin (Shanghai, China). Thiacetamide (CH_3CSNH_2, 99.5%) and 1,5-Diphenylcarbazide ($C_{13}H_{14}N_4O$, 98%) purchased from Beijing Balinway Technology Co. Ltd. HCP331N carbon cloth (0.35 mm in thickness) was obtained from Shanghai Hesen Electric Co. Ltd.

2.2. Synthesis of CuS nanocrystals

The one-step hydrothermal method is used to make the CuS nanocrystals self-growth on the carbon cloth substrates. First, the carbon cloth needs to be pretreated. The carbon cloth was cut to 3×4 cm^2 and soaked in acetone for 12 h to remove the surface organic impurities, then cleaned with deionized water. Next, 0.4 g $CuSO_4 \cdot 5 H_2O$ and 0.4 g CH_4N_2S were dissolved in 60 mL of deionized water (conductivity ≤ 0.1 μs/cm) and ultrasonically stirred to ensure a homogeneous dispersion of the solution. Thereafter, transfer the pretreated carbon cloth and the mixture to the polytetrafluoroethylene (PTFE) hydrothermal synthesis reactor and reacted at 180°C for 12 h. The synthesized material was rinsed and dried at 80°C. Finally, the carbon cloth electrodes loaded with CuS nanocrystals were obtained.

2.3. Cathodic tuning of CuS nanocrystals

All the electrochemical experiments were performed in a three-electrode system with Ag/AgCl electrodes as reference electrodes and Pt mesh as counter electrodes, and the CuS electrode as working electrode. All solutions were evenly dispersed by ultrasound for 10 min before use, and the solution was stirred at a constant speed during short-term cathodic tuning and Cr(VI) reduction. The electrolyte during cathode tuning was 50 mL of 0.5 M Na_2SO_4 solution. The synthesized CuS cathode was tuned for electrical stimulation for 1, 2, 3, 4 and 5 min

at the potentials of −0.6 V, −0.8 V, −1.0 V, −1.2 V, and −1.4 V. Next, the cathodic tuned CuS (C-tuned CuS) was transferred to 50 mL of 10 mg/L Cr(VI) solution and timed sampling was started.

2.4. Determination of the Cr(VI)

Determination of Cr(VI) in samples by ultraviolet-visible spectrophotometry (UV–VIS spectrophotometer, U-3900 H, Hitachi, Japan). 0.1 g of CH_3CSNH_2 was dissolved in a mixture of 5 mL of CH_3COCH_3 and 5 mL of deionized water and finally sonicated for 5 min to prepare the UV chromogenic agent. 0.5 mL chromogenic agent and 0.5 mL sample were evenly mixed in 5 mL centrifuge tube, 1 mL 2 M H_2SO_4 was injected into the mixture, and then deionized water was used for constant volume to 5 mL. Test the absorbance of the sample at a fixed wavelength of 540 nm, and calculate the corresponding Cr(VI) concentration of each samples through the absorbance value of the standard sample curve.

2.5. Characterization

The surface morphology imaging, elemental mapping images and microstructure of CuS before and after cathodic tuning were obtained using field-emission scanning electrom microscopy (SEM, S-4800, Hitachi Tokyo, Japan) and transmission electron microscopy (TEM, JEOL3010, JEOL Ltd., Akishima, Tokyo, Japan). The X-ray diffraction (XRD) patterns were tested by a Bruker D8 using a Cu Kα radiation source with the scan rate of 2.5° min^{-1} at 40 kV and 40 mA. X-ray photoelectron spectroscopy (XPS) was performed using a VG Escalab 250 spectrometer with an Al anode (Al-Kα=1486.7 eV) radiation source and peak positions were corrected by the C 1 s spectrum at 284.8 eV. XRD and XPS were used to analyse the crystal structure and elemental valence states of CuS before and after cathodic tuning.

In situ Raman was used to analyze bond length changes in CuS crystals under cathodic tuning. The schematic diagram of the apparatus is shown in Fig. S2. In-situ Raman spectra were recorded on a Raman microscope (NR-1800, JASCO) using a 514.5-nm argon ion laser with a temperature control table. The samples were fixed onto the substrate and then covered by an Au electrode to avoid a mechanical disturbance, and voltages can be applied at the both ends of the electrode under a vacuum system. The Raman spectra are obtained under different applied voltages. The corresponding two-electrode voltage and three-electrode potential (Ag/AgCl as reference electrode) conversions are shown in Table S1 and Table S2.

2.6. Theoretical arithmetic

The first-principles calculations were performed using the Vienna ab initio simulation package (VASP). The ion-electron interactions were described by the projector augmented wave (PAW) method. The exchange-correlation energy was modeled by generalized gradient approximation in the Perdew-Burke-Ernzerhof (GGA-PBE) form. The energy cutoff of 500 eV was used for the plane-wave basis set and the self-consistent convergence criteria imposed on force and energy were set at 0.01 eV/Å and 10^{-5} eV, respectively. [25] A $2 \times 2 \times 1$ supercell of CuS was constructed for the geometry optimization and electronic structure calculation. A $5 \times 5 \times 5$ Monkhorst-Pack k-point mesh was used. The van der Waals (vdW) interactions were described using the empirical correction in Grimme's method (DFT+D3). A vacuum space exceeding 15 Å was employed to avoid the interaction between two periodic units.

The free-energy change (ΔG) of each elementary reaction was calculated with the spin-polarization, as shown in the Eq 1:

$$\Delta G = \Delta E + \Delta EZPE - T\Delta S + \Delta GpH + \Delta GU \qquad (1)$$

Where ΔE is the difference between the adsorption energies of a given
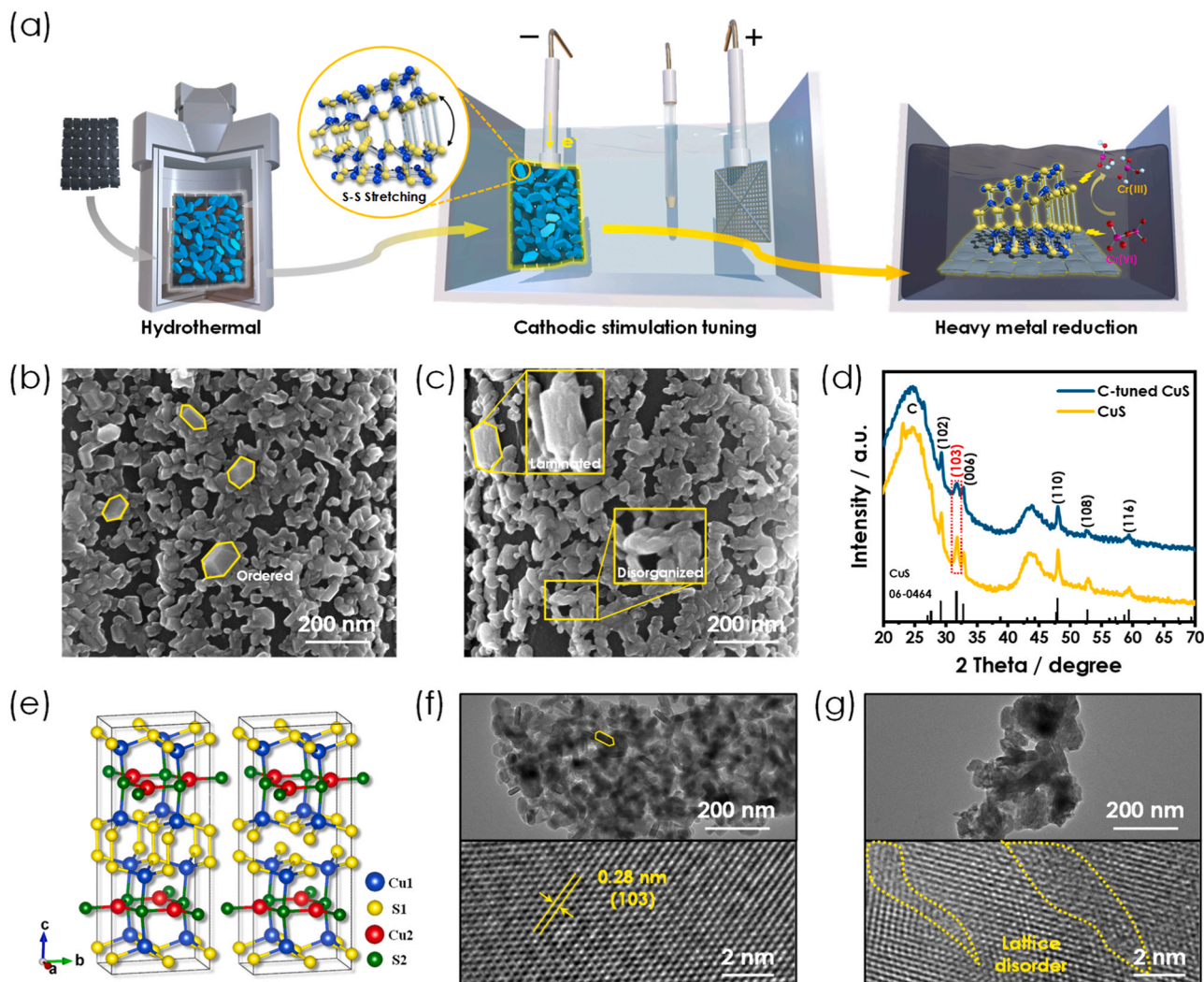
Fig. 1. (a) Schematic diagram of the preparation and application of C-tuned CuS. SEM images of (b) CuS and (c) C-tuned CuS. (d) XRD pattern of CuS before and after cathode tuning. (e) CuS cell diagram before and after S-S bond breakage. HRTEM images of (f) CuS and (g) C-tuned CuS.

group, $\Delta EZPE$ and ΔS are the differences in the zero-point energy and the change in entropy between the adsorbed state and the free-standing state, respectively; T is the temperature (T= 298.15 K), ΔGU is the contribution of the electrode potential (U) to shift the free energy ΔG at the applied U, and ΔGpH is the correction of the H^+ free energy due to the influence of the H^+ concentration ($\Delta GpH = 2.303 \times kBT \times pH \approx 0.059 \times pH$, where kB is the Boltzmann constant and the pH is assumed to be 0 in this work).

3. Results

### 3.1. Analysis of lattice distortion and S-S bond stretching of C-tuned CuS

The process of CuS electrode from synthesis to application is shown in Fig. 1a. First, we synthesized regular hexagonal CuS nanocrystals on carbon cloth substrate using a simple one-step hydrothermal method. Then, the synthesized CuS was then electrically stimulated for a short time to obtain C-tuned CuS. Finally, the C-tuned CuS were placed in Cr (VI)-containing wastewater for rapid Cr(VI) reduction. Because of the integration of the material and substrate, it is better recycled and less likely to cause secondary contamination than powder. The SEM analysis of the synthesized CuS nanocrystals in Fig. 1b shows that the crystals are in the form of regular freestanding hexagons. By contrast, the C-tuned CuS crystals partially show lamellar exfoliation and irregular

aggregation (Fig. 1c). This delamination morphology is due to partial S1-S1 bond breakage (Fig. 1e). The XRD (Fig. 1d) analysis shows that six characteristic peaks at $2\theta = 29.3°$, $31.7°$, $32.8°$, $47.9°$, $52.7°$ and $59.3°$ matched with CuS {102}, {103}, {006}, {110}, {108} and {116} face, [26,27] where the height of the characteristic peak of the {103} face is significantly reduced after cathode tuning. This implies that the breakage of the S-S bonds can cause the longitudinal (c-axis) collapse of the CuS crystal.

The TEM image (Fig. 1f) demonstrates the rgular ong hexagonal crystal aggregates of CuS, with sizes concentrated in the range of 20–100 nm (Fig. S4a and b). The cathode-tuned CuS no longer has clear crystal boundaries (Fig. 1g). The high-resolution TEM (HRTEM) indicates that the atomic arrangement of the {103} face in CuS is ordered, while the C-tuned CuS shows an ordered and disordered crossover, as in the reduced height of the {103} face characteristic peak in XRD. [28–30] The XPS tests of CuS before and after cathode tuning showed no significant valence change. The XPS peaks of Cu $2p_{3/2}$ are at 932.1 eV and 932.8 eV, while peaks of Cu $2p_{1/2}$ are at 952.1 eV and 952.8 eV, showing a Cu^{2+} (Fig. S5a). The S 2p peaks are at 161.2 eV and 162.1 eV, derived from S $2p_{3/2}$ and S $2p_{1/2}$ of S^{2-}, the binding energies positioned at 163.2 eV and 163.8 eV are derived from S $2p_{3/2}$ and S $2p_{1/2}$ of $(S_2)^{2-}$ (Fig. S5b). [31,32] To investigate the strain pattern of CuS under electrical tuning, in situ Raman was used to characterize the variations of bonds in CuS
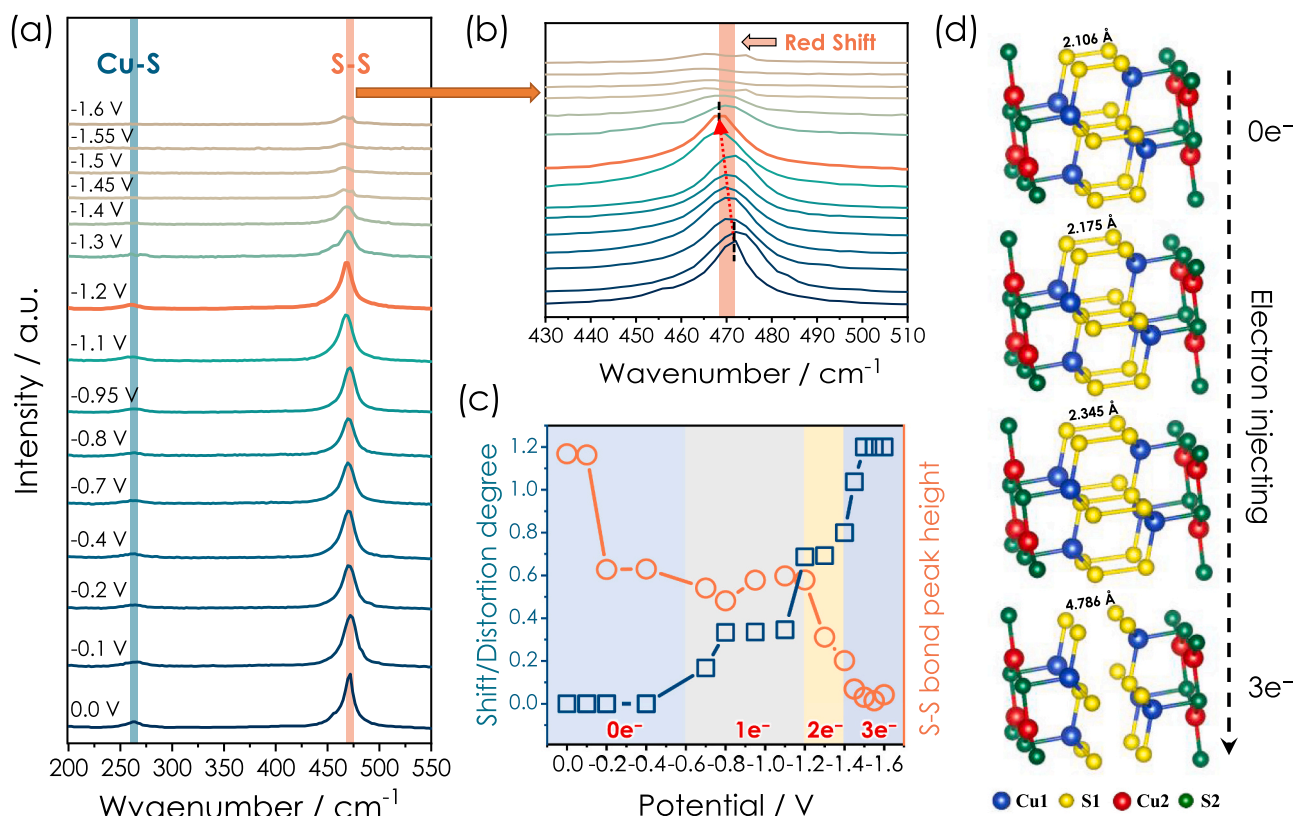
Fig. 2. (a) In-situ Raman spectra of CuS at different potentials. (b) Amplified in-situ Raman spectra of S-S bonds. (c) Correspondence between the degree of CuS distortion (%) and the peak height of S-S bond at different potentials. (d) Density functional theory analyzes the bond lengths of S-S bonds in CuS cells with different number of electron injections.

Table 1
Change of the bond length of the CuS under different amounts of electron injection.

Electrons	0	1	2	3
Cu1−S1 (Å)	2.305	2.399	2.498	2.288
Cu1−S2 (Å)	2.387	2.463	2.571	3.901
Cu2−S2 (Å)	2.199	2.284	2.392	2.288
S1−S1 (Å)	2.106	2.175	2.345	4.786 (Broken)

crystals under different potentials. Fig. 2a displays the normalized CuS in situ Raman spectra at 0.0 V to −1.6 V potential, in which the typical Raman peaks at 472.0 cm^{-1} and 270.0 cm^{-1} correspond to the vibrational (stretching) modes of the S-S bonds and the Cu-S bonds. [33–35] The peak height at 472.0 cm^{-1} and 270.0 cm^{-1} remains unchanged at the potential from 0.0 V to −1.2 V but decreases sharply from −1.3 V to −1.6 V. When the CuS crystal structure is broken at high potentials, the atomic vibrations of the S-S and Cu-S bonds clearly change to Raman disappearance. In addition, the S-S bonds at 472.0 cm^{-1} rapidly downshifts first from 472.0 cm^{-1} (0.0 V) to 469.7 cm^{-1} (−0.7 V), in to 467.4 cm^{-1} (−1.2 V), and finally anchored at 465.1 cm^{-1} starting from −1.4 V (Fig. 2b). This obvious Raman peak shift solidly supports that the stretching of the S-S bonds inside the CuS crystal can be effectively controlled under potential tuning. Fig. 2c integration of the distortion patterns of CuS crystals at different potentials based on the variation of the peak heights (orange curve) and the light wave numbers (cm^{-1}, blue curve) of the S-S bonds. The orange curve reveals that the peak height of the S-S bonds undergoes a three-step change. The first decrease of the peak height is at −0.1 V, the second obvious decrease is at −1.2 V, and the S-S bonds peak nearly disappears when over −1.5 V. Obviously the higher the potential the more serious the destruction of the S-S bonds. The blue curve indicates four stages of the S-S peak shifting in response

to the negative potential, there is 0.0 V to −0.6 V (stage 1), −0.7 V to −1.1 V (stage 2), −1.2 V to −1.4 V (stage 3), and over −1.5 V (stage 4), respectively. Taken together, it is clear that −1.2 V is the optimal choice, this is considering that this potential allows for highly tuned S-S bonds without extensive disruption of the CuS structure.

The stretching of bond lengths in CuS when 0–3 electrons are injected were calculated by density functional theory (DFT). The density of states (Fig. S7) and the energy band structure (Fig. S8) of CuS show that the orbitals above the Fermi energy level are contributed by both Cu and S. Therefore, injecting electrons into the CuS cell leads to a bond lengthening. Table 1 shows the bond lengths in CuS with different electron-injection. When 0–2 electrons are injected into CuS, both Cu-S and S-S bonds are lengthened due to the electron injection, where the S-S bond changed from 2.106 Å to 2.345 Å (Fig. 2d). However, the excess electrons (3 electron) cause the S-S bond to break and CuS structure is mutated, showing the structure of S changes from sp3 to sp2. Meanwhile, the distance between the two S atoms is 4.786 Å.

From the above discussion, it can be obtained that the four-stage shift of the in-situ Raman corresponds completely to the four-step electron injection of the theoretical calculation. Therefore, the four-stage distortion of CuS nanocrystals (or the four-stage stretching of S-S bonds) is summarized. Stage 1: from 0.0 V to −0.6 V (0 electrons/single cell), at lower potentials, the number of free electrons hardly affects the structure due to electron escape. Stage 2: from −0.7 V to −1.1 V (1 electron/single cell), the first stretching of the S-S bonds due to a further increase of free electrons. Stage 3: from −1.2 V to −1.4 V (2 electrons/ single cell), as the free electrons continue to increase, the electrostatic attraction between the S nucleus and the electrons approaches equilibrium, at which point the S-S bonds stretch to the limit. Stage 4: over −1.5 V (3 electrons/single cell), an excess of electrons causes the S-S bonds to break. To summarize, the precision tuning of the cathodic potential can effectively control the degree of distortion of the S-S bonds
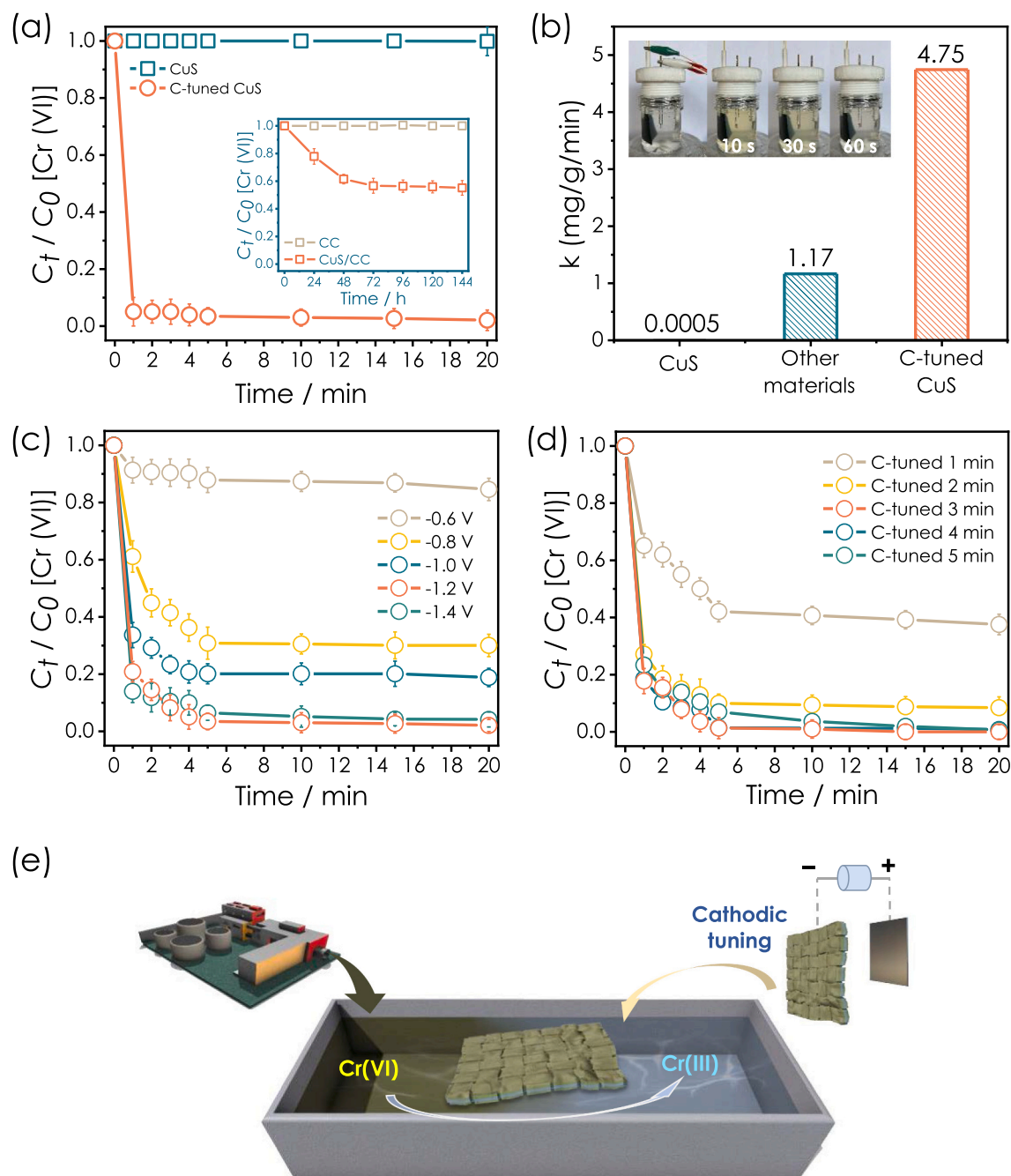
Fig. 3. (a) Reduction performance of CuS and C-tuned CuS to Cr(VI) (inset: Reduction performance of carbon cloth and CuS to Cr(VI) under natural conditions over 6 days). (b) Comparison of the reduction rates of Cr(VI) by CuS, some commercial reducing agents (Table S3), and C-tuned CuS (inset: digital image of Cr(VI) reduction by C-tuned CuS in one minute). Exploration of the optimization of (c) cathodic tuning potential and (d) time. (e) Application schematic of "Plug and Play" strategy.

in CuS nanocrystals.

3.2. Detoxification of Cr(VI) by C-tuned CuS

Fig. 3a displays the reduction performance of CuS and C-tuned CuS for Cr(VI). The inset in Fig. 3a indicates that CuS without cathodic tuning can only reduce 45% of Cr(VI) over a six-day period. In the contrast, the C-tuned CuS can reduce 95% of Cr(VI) within 1 min, with a reduction rate 9500 times faster than that of CuS (Fig. 3b), which is a dramatic increase in reducibility and rate. We further compared the Cr(VI) reduction rate in this study with other Cr(VI) removal materials reported in recent studies and found that C-tuned CuS was more advantageous in terms of reduction rates. The details of comparative data

can be found in Table S3 in the SI.

We further optimized the applied potential and tuning time. Fig. 3c investigates the reduction performance of CuS for Cr(VI) under different cathodic potential tuning. It is firstly obvious that when the potential is increased from −0.6 V to −0.8 V, the performance has an extremely significant improvement compared to other potentials. Secondly, the increase in potential (from −0.6 V to −1.2 V) favors the rapid tuning of CuS to its strongest state to reduce Cr(VI). Finally, too high potential (−1.4 V) seriously damages the structure of CuS and decreases its reduction performance. Through the above analysis, the optimization of the potential can be divided into four stages, which is completely consistent with the theoretical calculations and in-situ Raman results in Fig. 2. Next, the tuning state of CuS was investigated for different
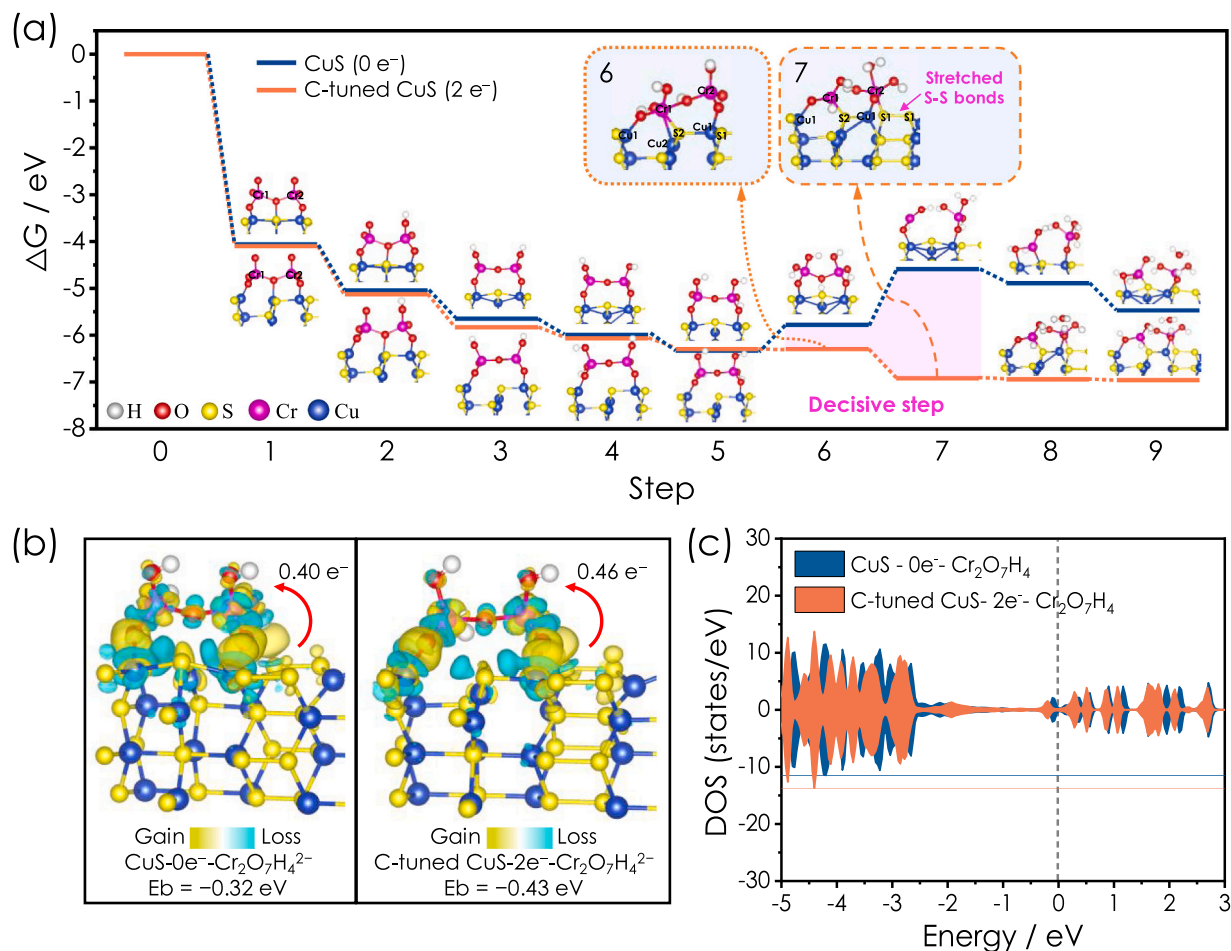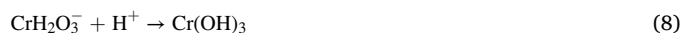
Fig. 4. (a) DFT modeling calculated the free energy landscape and the optimized structure of the intermediates in the reduction of Cr(VI) by CuS and C-tuned CuS. Calculated (b) charge density difference and (c) DOS for $Cr_2O_7H_4^{2-}$ adsorption by CuS and C-tuned CuS.

electrical stimulation times. Clearly, Fig. 3d indicates that at the same potential, an increase in time favors the accumulation of electrons in the CuS, but not the longer the time the better the performance. Therefore, a suitable electrical stimulation time is favorable for tuning the electronic state in CuS, and it is obvious that 3 min is optimal.

With the above integration, we demonstrate a plug and play strategy in Fig. 3e. Firstly, the wastewater containing Cr(VI) is collected in a device. Then, the CuS is rapidly activated to C-tuned CuS, and placed into wastewater to treat the Cr(VI). Finally, the Cr(III) is precipitated and recovered. This application strategy maximizes the reduction capacity of the materials and avoids oxidative losses during transportation. In addition, it has the advantages of easy recycling and less likely to cause secondary pollution.

3.3. DFT analysis of Cr(VI) reduction process

To further understand the reduction process of $Cr_2O_7^{2-}$, DFT modeling was performed by the VASP software. [36,37] The computational hydrogen electrode model was used to calculate the free energy landscape for the reduction of $Cr_2O_7^{2-}$. In this model, one electron-proton pair is transferred at each step. The calculated free energy landscape and the optimized structure of the intermediates are shown in Fig. 4a. And the relevant chemical equations are given in Eqs. (2)-(9).

$$Cr_2O_7^{2-} + H^+ + e^- \rightarrow Cr_2HO_7^{2-} \tag{2}$$

$$Cr_2HO_7^{2-} + H^+ + e^- \rightarrow Cr_2H_2O_7^{2-} \tag{3}$$

$$Cr_2H_2O_7^{2-} + H^+ + e^- \rightarrow Cr_2H_3O_7^{2-} \tag{4}$$

$$Cr_2H_3O_7^{2-} + H^+ + e^- \rightarrow Cr_2H_4O_7^{2-} \tag{5}$$

$$Cr_2H_4O_7^{2-} + H^+ + e^- \rightarrow Cr_2H_5O_7^{2-} \tag{6}$$

$$Cr_2H_5O_7^{2-} + H^+ + e^- \rightarrow CrH_4O_4^- + CrH_2O_3^- \tag{7}$$

$$CrH_2O_3^- + H^+ \rightarrow Cr(OH)_3 \tag{8}$$

$$CrH_4O_4^- + H^+ \rightarrow Cr(OH)_3 + H_2O \tag{9}$$

In the reduction mode of CuS, the first step is that $Cr_2O_7^{2-}$ adsorbed on the CuS surface, which is a exothermic process, and exothermic by 4.06 eV, suggesting that the adsorption of $Cr_2O_7^{2-}$ on CuS is thermodynamically favorable. In steps two through five, successively four protons are transferred to four O atoms bonded to only one Cr. Each electron-proton transfer process is calculated to be thermodynamically favorable. In the sixth step, a proton is transferred on the O to which Cr1 and Cr2 are co-bonded. However, the reaction free energy is elevated by 0.55 eV in this step, indicating that it is a heat-absorbing reaction, which is thermodynamically unfavorable. In the seventh step, $Cr_2H_5O_7^{2-}$ splits into a $CrH_4O_4^-$ group and a $CrH_2O_3^-$ group (Eq. (7)). This is a heat-absorbing process that absorbs 1.19 eV, suggesting that the splitting of $Cr_2H_5O_7^{2-}$ on the CuS surface is thermodynamically unfavorable. Therefore, the reaction energy is climbing when adding the 5th and 6th protons without external energy intervention, indicating that spontaneous reduction of Cr(VI) is not possible in this case. [38]

In the reduction mode of C-tuned CuS, the first five steps of Cr(VI) hydrogenation reduction are similar to the model of CuS, while there is a significant difference from the sixth step onwards. In the sixth step, a

proton is transferred to O co-bonded to Cr1 and Cr2, and Cr1 is bonded to S2 and Cu2 in C-tuned CuS, and the reaction energy is not elevated. In the seventh step, $Cr_2H_5O_7^{2-}$ splits into a $CrH_4O_4^-$ group and a $CrH_2O_3^-$ group, Cr1 is disconnected from Cu2, and Cr2 is bonded to Cu1 and S1. From the calculated free energy, this step is markedly exothermic, with a thermodynamically favorable reaction energy drop of 0.63 eV. Obviously, the decrease in reaction energy is attributed to the direct bonding of Cr to Cu and S in C-tuned CuS. Resulting in a shift from O-mediated long-process electron transfer to direct electron transfer, thus favoring spontaneous Cr(VI) reduction. In the reduction mode of C-tuned CuS, each electron-proton transfer process was calculated to be thermodynamically favorable. Comparing the adsorption of CuS and C-tuned CuS on $Cr_2O_7H_4^{2-}$, it can be found that the adsorption energy of C-tuned CuS on $Cr_2O_7H_4^{2-}$ is greater, which is favorable for obtaining more electrons from the substrate (Fig. 4b). Fig. 4c indicates that compared with CuS, the overall energy levels of C-tuned CuS are shifted to lower energy levels, which makes the LUMO orbitals of $Cr_2O_7H_4^{2-}$ closer to the Fermi energy level, which is more favorable for the import of e^-, and makes $Cr_2O_7H_4^{2-}$ easier to be reacted.

4. Conclusion

In this study, we tune the S-S bond of CuS by cathodic potential tuning, creating a new heavy metal reduction treatment strategy. C-tuned CuS exhibited ultra-fast reduction of Cr(VI), which was five orders of magnitude times faster than CuS and 4.06 times faster than some reported catalysts. The strain stretching and electronic activation states of S-S bond sites of CuS are effectively regulated by gradient potential control, and the electron-proton transfer process is thermodynamically favorable to proceed spontaneously, thus the activated state of CuS can significantly lower the Cr(VI) reduction energy barrier. We found that the S atoms in the high-energy state can undergo direct electron transfer with the Cr atoms, avoiding the O atoms as intermediates to generate energy level losses. This activating S atomic site strategy by cathodic tuning provides a new perspective for heavy metal reduction. In addition, this "plug-and-play" strategy avoids the generation of slag and the oxidative loss of the reduction reagent during transportation.

CRediT authorship contribution statement

Wenwei Li: Validation. **Xubiao Luo:** Writing – review & editing, Supervision, Resources, Project administration, Funding acquisition, Formal analysis. **Xianchuan Xie:** Validation, Software. **Guangzhen Liu:** Data curation, Conceptualization, Methodology, Project administration, Writing – review & editing. **Liming Yang:** Conceptualization, Investigation, Methodology, Writing – original draft. **Hui Shi:** Writing – original draft. **Penghui Shao:** Supervision, Formal analysis. **Tian Liu:** Writing – review & editing, Supervision, Formal analysis. **Zhiyan Guo:** Validation, Investigation. **Zhenglin Chen:** Software, Formal analysis, Data curation.

Declaration of Competing Interest

The authors declare that they have no known competing financial interests or personal relationships that could have appeared to influence the work reported in this paper.

Data Availability

Data will be made available on request.

Acknowledgments

Appendix A. Supporting information

Supplementary data associated with this article can be found in the online version at doi:10.1016/j.apcatb.2024.123898.

References

[1] J. Long, Y. Zheng, S. Zha, J. Huang, D. Peng, G. Zhang, H. Li, Freshly formed elemental sulfur-sulfidated zero-valent manganese for enhanced chromium (VI) removal from wastewater, Chem. Eng. J. 472 (2023) 144714, https://doi.org/10.1016/j.cej.2023.144714.

[2] L. Kong, X. Peng, X. Hu, J. Chen, Z. Xia, UV-light-induced aggregation of arsenic and metal sulfide particles in acidic wastewater: the role of free radicals, Environ. Sci. Technol. 52 (18) (2018) 10719–10727, https://doi.org/10.1021/acs.est.8b03265.

[3] J. Long, Y. Zheng, S. Zha, J. Huang, D. Peng, G. Zhang, H. Li, Freshly formed elemental sulfur-sulfidated zero-valent manganese for enhanced chromium (VI) removal from wastewater, Chem. Eng. J. 472 (2023) 144714, https://doi.org/10.1016/j.cej.2023.144714.

[4] T. Jia, B. Zhang, L. Huang, S. Wang, C. Xu, Enhanced sequestration of Cr (VI) by copper doped sulfidated zerovalent iron (SZVI-Cu): Characterization, performance, and mechanisms, Chem. Eng. J. 366 (2019) 200–207, https://doi.org/10.1016/j.cej.2019.02.058.

[5] S. Huang, C. Xu, Q. Shao, Y. Wang, B. Zhang, B. Gao, P.G. Tratnyek, Sulfide-modified zerovalent iron for enhanced antimonite sequestration: characterization, performance, and reaction mechanisms, Chem. Eng. J. 338 (2018) 539–547, https://doi.org/10.1016/j.cej.2018.01.033.

[6] M. Asadi, K. Kim, C. Liu, A.V. Addepalli, P. Abbasi, P. Yasaei, A. Salehi-Khojin, Nanostructured transition metal dichalcogenide electrocatalysts for CO2 reduction in ionic liquid, Science 353 (6298) (2016) 467–470, https://doi.org/10.1126/science.aaf4767.

[7] Y. Zhao, H. Wu, Y. Wang, L. Liu, W. Qin, S. Liu, M. Qin, Sulfur coordination engineering of molybdenum single-atom for dual-functional oxygen reduction/evolution catalysis, Energy Storage Mater. 50 (2022) 186–195, https://doi.org/10.1016/j.ensm.2022.05.015.

[8] L. Omann, C.D.F. Königs, H.F. Klare, M. Oestreich, Cooperative catalysis at metal–sulfur bonds, Acc. Chem. Res. 50 (5) (2017) 1258–1269, https://doi.org/10.1021/acs.accounts.7b00089.

[9] P. Abbasi, M. Asadi, C. Liu, S. Sharifi-Asl, B. Sayahpour, A. Behranginia, A. Salehi-Khojin, Tailoring the edge structure of molybdenum disulfide toward electrocatalytic reduction of carbon dioxide, ACS Nano 11 (1) (2017) 453–460, https://doi.org/10.1021/acsnano.6b06392.

[10] A. Nayeem, M.F. Ali, J.H. Shariffuddin, The recent development of inverse vulcanized polysulfide as an alternative adsorbent for heavy metal removal in wastewater, Environ. Res. 216 (2023) 114306, https://doi.org/10.1016/j.envres.2022.114306.

[11] J. Xu, W. Zhong, X. Zhang, X. Wang, X. Hong, H. Yu, Triggering the channel-sulfur sites in 1T'-ReS2 cocatalyst toward splendid photocatalytic hydrogen generation, Small (2023) 2303960, https://doi.org/10.1002/smll.202303960.

[12] X. Hu, L. Yan, L. Ding, N. Zheng, D. Li, T. Ji, N. Chen, J. Hu, Structural regulation and application of transition metal dichalcogenide monolayers: Progress and challenges, Coord. Chem. Rev. 499 (2024) 215504, https://doi.org/10.1016/j.ccr.2023.215504.

[13] A. Sohn, C. Kim, J.H. Jung, J.H. Kim, K.E. Byun, Y. Cho, H.J. Shin, Precise layer control and electronic state modulation of a transition metal dichalcogenide via phase-transition-induced growth, Adv. Mater. 34 (48) (2022) 2103286, https://doi.org/10.1002/adma.202103286.

[14] W. Liu, C. Luo, S. Zhang, B. Zhang, J. Ma, X. Wang, W. Lv, Cobalt-doping of molybdenum disulfide for enhanced catalytic polysulfide conversion in lithium–sulfur batteries, ACS Nano 15 (4) (2021) 7491–7499, https://doi.org/10.1021/acsnano.1c00896.

[15] L. Wang, X. Liu, J. Luo, X. Duan, J. Crittenden, C. Liu, X. Duan, Self-optimization of the active site of molybdenum disulfide by an irreversible phase transition during photocatalytic hydrogen evolution, Angew. Chem. 129 (26) (2017) 7718–7722, https://doi.org/10.1002/anie.201703066.

[16] X. Liu, Y. Li, Z. Chen, H. Yang, S. Wang, Z. Tang, X. Wang, Recent progress of COFs membranes: design, synthesis and application in water treatment, Eco-Environ. Health (2023), https://doi.org/10.1016/j.eehl.2023.07.001.

[17] X. Zhang, Z. Zhao, W. Zhang, G. Zhang, D. Qu, X. Miao, S. Sun, Z. Sun, Surface defects enhanced visible light photocatalytic H2 production for Zn-Cd-S solid solution, Small 12 (6) (2016) 793–801, https://doi.org/10.1002/smll.201503067.

[18] L. Lv, R. Lu, J. Zhu, R. Yu, W. Zhang, E. Cui, X. Chen, Y. Dai, L. Cui, J. Li, L. Zhou, W. Chen, Z. Wang, L. Mai, Coordinating the edge defects of bismuth with sulfur for enhanced CO2 electroreduction to formate, Angew. Chem. (2023) e202303117, https://doi.org/10.1002/ange.202303117.

[19] Z. Chen, G. Liu, W. Cao, L. Yang, L. Zhang, S. Zhang, J. Zou, R. Song, W. Fan, S. Luo, D.D. Dionysiou, Amorphous low-coordinated cobalt sulphide nanosheet electrode for electrochemically synthesizing hydrogen peroxide in acid media, Appl. Catal. B: Environ. 334 (2023) 122825, https://doi.org/10.1016/j. apcatb.2023.122825.

[20] Z. Chen, G. Liu, S. Yu, L. Yang, L. Zheng, Z. Wei, S. Luo, Amorphous cobalt sulphide introduced atomic H*/H$^+$ for H$_2$O$_2$ electrosynthesis and enhanced Fe(II) regeneration in electro-Fenton process at macroneutral pH. Chem. Eng. J. (2023) 145581 https://doi.org/10.1016/j.cej.2023.145581.

[21] F. Xiong, Y. Fan, S. Tan, L. Zhou, Y. Xu, C. Pei, Q. An, L. Mai, Magnesium storage performance and mechanism of CuS cathode, Nano Energy 47 (2018) 210–216, https://doi.org/10.1016/j.nanoen.2018.02.060.

[22] Z.G. Yang, Z.G. Wu, W.B. Hua, Y. Xiao, G.K. Wang, Y.X. Liu, X.D. Guo, Hydrangea-Like CuS with Irreversible Amorphization Transition for High-Performance Sodium-Ion Storage, Adv. Sci. 7 (11) (2020) 1903279, https://doi.org/10.1002/advs.201903279.

[23] L. Fang, T. Huang, H. Lu, X.L. Wu, Z. Chen, H. Yang, S. Wang, Z. Tang, Z. Li, B. Hu, X. Wang, Biochar-based materials in environmental pollutant elimination, H$_2$ production and CO$_2$ capture applications, Biochar 5 (1) (2023) 42, https://doi.org/10.1007/s42773-023-00237-7.

[24] G.G. Naumis, S. Barraza-Lopez, M. Oliva-Leyva, H. Terrones, Electronic and optical properties of strained graphene and other strained 2D materials: a review, Rep. Prog. Phys. 80 (9) (2017) 096501, https://doi.org/10.1088/1361-6633/aa74ef.

[25] Q. Ge, X. Feng, R. Wang, R. Zheng, S. Luo, L. Duan, H. Chen, Mixed redox-couple-involved chalcopyrite phase CuFeS$_2$ quantum dots for highly efficient Cr (VI) removal, Environ. Sci. Technol. 54 (13) (2020) 8022–8031, https://doi.org/10.1021/acs.est.0c01018.

[26] Y. Wang, D. Chao, Z. Wang, J. Ni, L. Li, An energetic CuS–Cu battery system based on CuS nanosheet arrays, ACS Nano 15 (3) (2021) 5420–5427, https://doi.org/10.1021/acsnano.1c00075.

[27] X. Xin, Y. Song, S. Guo, Y. Zhang, B. Wang, J. Yu, X. Li, In-situ growth of high-content 1T phase MoS$_2$ confined in the CuS nanoframe for efficient photocatalytic hydrogen evolution, Appl. Catal. B: Environ. 269 (2020) 118773, https://doi.org/10.1016/j.apcatb.2020.118773.

[28] M. Geng, H. Yang, C. Shang, The Multi-Functional Effects of CuS as Modifier to Fabricate Efficient Interlayer for Li-S Batteries, Adv. Sci. 9 (35) (2022) 2204561, https://doi.org/10.1002/advs.202204561.

[29] Z. Zheng, P. Yu, H. Cao, M. Cheng, T. Zhou, L.E. Lee, L. Ma, Starch capped atomically thin CuS nanocrystals for efficient photothermal therapy, Small 17 (47) (2021) 2103461, https://doi.org/10.1002/smll.202103461.

[30] L. Yao, Z. Shen, Z. Ji, Y. Hu, D. Tang, G. Zhao, X. Wang, Cr (VI) detoxification and simultaneous selective recovery of Cr resource from wastewater via photochemical extraction using biomass, Sci. Bull. 67 (21) (2022) 2154–2157, https://doi.org/10.1016/j.scib.2022.10.013.

[31] K. Cho, S.H. Han, M.P. Suh, Copper–organic framework fabricated with CuS nanoparticles: synthesis, electrical conductivity, and electrocatalytic activities for oxygen reduction reaction, Angew. Chem. 128 (49) (2016) 15527–15531, https://doi.org/10.1002/ange.201607271.

[32] J. Zhang, Q. Lei, Z. Ren, X. Zhu, J. Li, Z. Li, L. Fu, A superlattice-stabilized layered CuS anode for high-performance aqueous zinc-ion batteries, ACS Nano 15 (11) (2021) 17748–17756, https://doi.org/10.1021/acsnano.1c05725.

[33] J.S. Nam, J.H. Lee, S.M. Hwang, Y.J. Kim, New insights into the phase evolution in CuS during lithiation and delithiation processes, J. Mater. Chem. A 7 (19) (2019) 11699–11708, https://doi.org/10.1039/C9TA03008E.

[34] G. Liu, Z. Chen, F. Luo, T. Liu, X. Xi, Z. Wang, Z. Gao, P. Shao, D. Wu, X. Luo, L. Yang, One-step nickel-cobalt alloy electrodeposition from spent lithium-ion battery via synergistic pH adjustment and Mn^{2+} supplementation, Sep. Purif. Technol. 314 (2023) 123581, https://doi.org/10.1016/j.seppur.2023.123581.

[35] P. Liu, Y. Huang, J. Yan, Y. Yang, Y. Zhao, Construction of CuS nanoflakes vertically aligned on magnetically decorated graphene and their enhanced microwave absorption properties, ACS Appl. Mater. Interfaces 8 (8) (2016) 5536–5546, https://doi.org/10.1021/acsami.5b10511.

[36] G. Kresse, J. Furthmüller, Efficiency of ab-initio total energy calculations for metals and semiconductors using a plane-wave basis set, Comput. Mater. Sci. 6 (1) (1996) 15–50, https://doi.org/10.1016/0927-0256(96)00008-0.

[37] Y.X. Pan, Y. You, S. Xin, Y. Li, G. Fu, Z. Cui, J.B. Goodenough, Photocatalytic CO$_2$ reduction by carbon-coated indium-oxide nanobelts, J. Am. Chem. Soc. 139 (11) (2017) 4123–4129, https://doi.org/10.1021/jacs.7b00266.

[38] L. Yao, Y. Hu, Y. Zou, Z. Ji, S. Hu, C. Wang, Ping Zhang, H. Yang, Z. Shen, D. Tang, S. Zhang, G. Zhao, X. Wang, Selective and efficient photoextraction of aqueous Cr (VI) as a solid-state polyhydroxy Cr (V) complex for environmental remediation and resource recovery, Environ. Sci. Technol. 56 (19) (2022) 14030–14037, https://doi.org/10.1021/acs.est.2c03994.